

*The interplay of metal-atom ordering,
Fermi leveltuning and thermoelectric
properties in cobalt shandites $\text{Co}_3\text{M}_2\text{S}_2$
($M = \text{Sn}, \text{In}$)*

Article

Accepted Version

Corps, J., Vaqueiro, P. ORCID: <https://orcid.org/0000-0001-7545-6262>, Aziz, A., Grau-Crespo, R. ORCID: <https://orcid.org/0000-0001-8845-1719>, Kockelmann, W., Jumas, J.-C. and Powell, A. V. (2015) The interplay of metal-atom ordering, Fermi leveltuning and thermoelectric properties in cobalt shandites $\text{Co}_3\text{M}_2\text{S}_2$ ($M = \text{Sn}, \text{In}$). *Chemistry of Materials*, 27 (11). pp. 3946-3956. ISSN 1520-5002 doi: 10.1021/acs.chemmater.5b00801 Available at <https://centaur.reading.ac.uk/40312/>

It is advisable to refer to the publisher's version if you intend to cite from the work. See [Guidance on citing](#).

To link to this article DOI: <http://dx.doi.org/10.1021/acs.chemmater.5b00801>

Publisher: American Chemical Society

All outputs in CentAUR are protected by Intellectual Property Rights law, including copyright law. Copyright and IPR is retained by the creators or other

copyright holders. Terms and conditions for use of this material are defined in the [End User Agreement](#).

www.reading.ac.uk/centaur

CentAUR

Central Archive at the University of Reading

Reading's research outputs online

The Interplay of Metal-Atom Ordering, Fermi Level Tuning and Thermoelectric Properties in Cobalt Shandites $\text{Co}_3\text{M}_2\text{S}_2$ ($\text{M} = \text{Sn}, \text{In}$)

Jack Corps¹, Paz Vaquero^{2*}, Alex Aziz², Ricardo Grau-Crespo², Winfried Kockelmann³, Jean-Claude Jumas⁴ and Anthony V. Powell^{2*}.

¹Institute of Chemical Sciences, Heriot-Watt University, Edinburgh EH14 4AS, UK.

² Department of Chemistry, University of Reading, Whiteknights, Reading RG6 6AD, UK

³ STFC, Rutherford Appleton Laboratory, ISIS Facility, Didcot OX11 0QX, UK.

⁴ Institut Charles Gerhardt, UMR 5253, Université Montpellier II, F-34095, Montpellier 5, France.

ABSTRACT: A combination of structural, physical and computational techniques including powder X-ray and neutron diffraction, SQUID magnetometry, electrical and thermal transport measurements, DFT calculations and ^{119}Sn Mössbauer and X-ray photoelectron spectroscopies has been applied to $\text{Co}_3\text{Sn}_{2-x}\text{In}_x\text{S}_2$ ($0 \leq x \leq 2$) in an effort to understand the relationship between metal-atom ordering and physical properties as the Fermi level is systematically varied. Whilst solid solution behavior is found throughout the composition region, powder neutron diffraction reveals that indium preferentially occupies an inter-layer site over an alternative kagome-like intra-layer site. DFT calculations indicate that this ordering, which leads to a lowering of energy, is related to the differing bonding properties of tin and indium. Spectroscopic data suggest that throughout the composition range $0 \leq x \leq 2$, all elements adopt oxidation states that are significantly reduced from expectations based on formal charges. Chemical substitution enables the electrical transport properties to be controlled through tuning of the Fermi level within a region of the density of states, which comprises narrow bands of predominantly Co d -character. This leads to a compositionally-induced double metal-to-semiconductor-to-metal transition. The marked increase in the Seebeck coefficient as the semiconducting region is approached leads to a substantial improvement in the thermoelectric figure of merit, ZT , which exhibits a maximum of $ZT = 0.32$ at 673 K. At 425 K, the figure of merit for phases in the region $0.8 \leq x \leq 0.85$ is amongst the highest reported for sulphide phases, suggesting these materials may have applications in low-grade waste heat recovery.

INTRODUCTION

Shandites are a family of structurally-related materials of general formula $A_3M_2X_2$ ($A = \text{Ni}, \text{Co}, \text{Rh}, \text{Pd}; M = \text{Pb}, \text{In}, \text{Sn}, \text{Tl}; X = \text{S}, \text{Se}$).¹ The structure (Space group: $R\bar{3}m$) consists of a kagome-like network of corner-sharing A_3 triangles, with M atoms located in sites of six-fold coordination by A (Figure 1). Each of the A_3 triangles is capped above or below the kagome sheets by an X atom. Two-dimensional sheets of A and M atoms are then stacked in an ABC sequence, generating trigonal antiprismatic inter-layer sites. M atoms are distributed over $M(2)$ sites in the kagome layers and $M(1)$ inter-layer sites.

Our investigations of shandite-related phases have focused on the effects of chemical substitution in $\text{Co}_3\text{Sn}_2\text{S}_2$. This is the only shandite-type phase to exhibit long-range magnetic order ($T_C = 177 \text{ K}$)² and it has been described as a type I_A half-metallic ferrromagnet.³ Band structure calculations³ on $\text{Co}_3\text{Sn}_{2-x}\text{In}_x\text{S}_2$ ($x = 0, 1, 2$) reveal that states in the vicinity of the Fermi level, E_F , are predominantly of Co d -character, giving rise to sharp, narrow bands. The highly structured density of states, $N(E)$, in the vicinity of E_F offers considerable scope for the design of high-performance thermoelectric materials by maximizing the Seebeck coefficient, S .⁴ As the Seebeck coefficient is related to the derivative of $N(E)$, at E_F , through the Mott relation,⁵ enhancements in S may be produced if E_F coincides with a sharp change in $N(E)$.⁶ The challenge lies in tuning the position of E_F to such a discontinuity in $N(E)$.

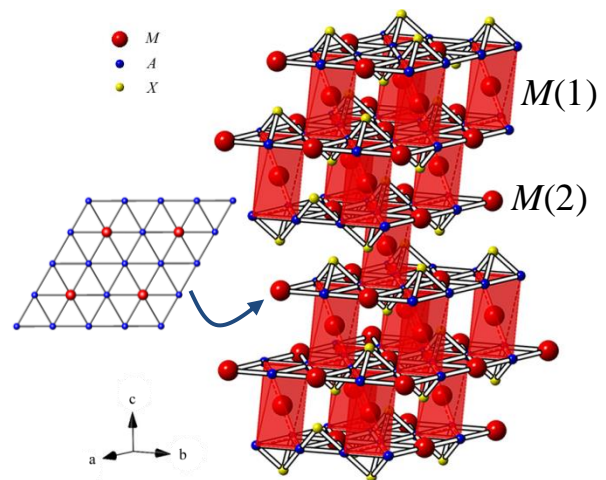


Figure 1. The shandite structure of $A_3M_2S_2$ containing $M(2)$ sites within a kagome-like layer and $M(1)$ inter-layer sites. A , M and S atoms are represented by blue, red and yellow circles respectively. $M(1)$ is located in trigonal antiprismatic sites, represented by shaded polyhedra. The kagome-like A_3M layer is shown as an inset.

Electron populations indicate metallic behavior for $\text{Co}_3\text{Sn}_{2-x}\text{In}_x\text{S}_2$ phases with $x = 0$ and 2, in accord with experiment, whilst DFT calculations on the stoichiometric phase

$\text{Co}_3\text{SnInS}_2$ predict semiconducting behavior for complete ordering of indium and tin over the $M(1)$ and $M(2)$ sites respectively. Conversely, if tin exclusively occupies the $M(1)$ sites, metallic behavior is predicted. We recently communicated preliminary results on the synthesis and low-temperature electrical transport properties of $\text{Co}_3\text{Sn}_{2-x}\text{In}_x\text{S}_2$ ($0 \leq x \leq 2$)⁷ that revealed an unusual double metal-to-semiconductor-to-metal transition as tin is progressively replaced by indium. However, this work raised a number of questions. In particular, since samples were characterized by powder X-ray diffraction, the indistinguishability of tin and indium precluded the establishment of the degree of ordering, which calculations suggest plays a key role in the electron transport properties.³ Furthermore, the formal oxidation states of the constituent elements of shandite-related materials continues to be a matter of debate, with several groups reaching different conclusions. For example, Gutlich et al.⁸ have formulated the nickel analogue as $\text{Ni}_3\text{Sn}^{2+}_2\text{S}^{2-}_2$. However for the cobalt analogue $\text{Co}_2\text{Sn}_2\text{S}_2$ and its substituted derivative, CoSnInS_2 , Rothballer et al.⁹ suggest, that the ^{119}Sn Mössbauer spectroscopy isomer shifts are close to those expected for zero-valent $\alpha\text{-Sn}$ and rutilite Sn(II) or Sn(IV) , leading to the suggestion of an intermediate state. By contrast, Umetani et al.,¹⁰ have proposed that cobalt is present in a mixed-valence (Co(0) , Co(II)) state in $\text{Co}_3\text{Sn}_2\text{S}_2$, whilst Skinner et al.¹¹ conclude that zero-valent nickel is present in $\text{Ni}_3\text{Pb}_2\text{S}_2$. Their careful XPS study reveals that rapid oxidation of the surface may occur under ambient conditions leading to changes in the spectral data. The data reveal that the $\text{Pb}(4f_{7/2})$ binding energy is within 0.15 eV of that of elemental lead but is 0.75 eV lower than that for PbS . However, the presence of Ni(0) and Pb(0) would not provide charge balance for divalent sulphur.

Here we exploit the contrast between tin and indium afforded by powder neutron diffraction, to establish the evolution with composition of cation partitioning over the $M(1)$ and $M(2)$ sites across the series $\text{Co}_3\text{Sn}_{2-x}\text{In}_x\text{S}_2$ ($0 \leq x \leq 2$) and compare the resulting distribution with the results of atomistic modeling. Complementary spectroscopic investigations by Mössbauer and XPS has provided insights into the formal oxidation state of the component elements and suggests that the behavior of this series is more akin to an intermetallic system than the ionic-covalent compound suggested by its formulation as a ternary sulphide. The composition-induced changes in electronic states have been probed by magnetic and transport property measurements and indicate that these materials are attractive candidates for thermoelectric energy recovery in the low to medium temperature range

EXPERIMENTAL

Samples corresponding to stoichiometries $\text{Co}_3\text{Sn}_{2-x}\text{In}_x\text{S}_2$ ($0 \leq x \leq 2$) were prepared from mixtures of elemental cobalt (350 mesh, Alfa, 99.95 %), tin (350 mesh, Alfa, 99.8%), indium (350 mesh, Alfa, 99.99 %) and sulphur (flakes, Aldrich, 99.99 %). The powders were ground in an agate pestle and mortar and sealed into evacuated ($<10^{-4}$ Torr) fused silica tubes. Intermediate regrinding was used to homogenize the samples between firings and the progress of each reaction was monitored by powder X-ray diffraction using a Bruker D8 Advance diffractometer ($\text{Cu-K}\alpha_1$: $\lambda = 1.54050 \text{ \AA}$) equipped with a LynxEye detector. The tin end-member phase ($x = 0$), was prepared according to the previously reported procedure² by heating the reaction mixture at 500 °C for 48 hours, followed by a second firing at 700 °C for 48 hours. The sample was

cooled to room temperature at 0.5 °C min^{-1} after each firing. The indium end-member of this series ($x = 2$) was prepared by increasing the temperature to 800 °C at 0.5 °C min^{-1} and holding at this temperature for 96 hours, prior to cooling at the same rate. This procedure was repeated three times. All mixed main group metal compositions were prepared by heating samples for three periods of 48 hours at 900 °C. All $\text{Co}_3\text{Sn}_{2-x}\text{In}_x\text{S}_2$ ($0 \leq x \leq 2$) phases are black powders.

Powder neutron diffraction data were collected at room temperature on the GEM diffractometer at the ISIS facility, Rutherford Appleton Laboratory. Data were collected for powdered samples of $\text{Co}_3\text{Sn}_{2-x}\text{In}_x\text{S}_2$ ($0 \leq x \leq 2$) contained in vanadium cans. Diffraction data for tin-rich samples were collected for 300 μA of beam current whilst those for indium-rich samples were collected for 400 μA . The increase in collection time was to compensate for the higher neutron absorption cross section of indium.

Samples for electrical and thermal transport property measurements were fabricated using a hot press constructed in-house. Approximately 1 g of sample was placed between two 13 mm diameter graphite anvils inside a graphite die. Under an inert nitrogen atmosphere, samples were heated to 720 °C under 60 bar. The load was released after 30 minutes prior to cooling the die to room temperature. In this way, pellets with $> 90\%$ of the theoretical density, as determined geometrically, were obtained. Ingots (approximately $8 \times 3 \times 1 \text{ mm}^3$) for electrical transport property measurements were cut using a low-speed diamond saw. Measurements of the electrical resistivity and Seebeck coefficient were performed simultaneously over the temperature range $303 \leq T/\text{K} \leq 673$ in 10 K steps, using a Linseis LSR3-800 instrument. A temperature gradient of 30 K was applied and a current of 100 mA was used.

Thermal diffusivity measurements were carried out over the temperature range $373 \leq T/\text{K} \leq 673$ in 50 K steps using an Anter Flashline 3000 instrument. Measurements were made on 13 mm diameter hot-pressed pellets of thickness 1 to 1.5 mm. The top and bottom surfaces of the pellets were coated with a thin layer of graphite to increase absorption and emission of the heat pulse.

Magnetic measurements were performed using a Quantum Design MPMS SQUID magnetometer. Approximately 30 mg of powdered sample were loaded at room temperature into gelatine capsules. Magnetization data were collected over the temperature range $2 \leq T/\text{K} \leq 300$, both after cooling in zero applied field (zfc) and in a measuring field (fc) of 1000 G. Data were corrected for the diamagnetism of the gelatine capsule and for intrinsic core diamagnetism. In addition, for selected samples, magnetization data were collected as a function of field at 5K, over the field range $0 \leq H/\text{kG} \leq 10$.

X-ray photoelectron spectroscopy (XPS) data were recorded for five samples in the $\text{Co}_3\text{Sn}_{2-x}\text{In}_x\text{S}_2$ ($0 \leq x \leq 2$) series at the Nexus facility, Newcastle University, UK. Ingots from hot-pressed pellets corresponding to $x = 0, 0.4, 1, 1.6$ and 2 were cleaned by sputtering for 600 s with monatomic Ar ions at 1 keV. Measurements were performed in the presence of a flood gun, which is a charge neutralization method that generates low energy electrons and Ar^+ ions near the vicinity of the surface.

^{119}Sn Mössbauer spectra were recorded in transmission mode and in constant acceleration mode using a $^{119\text{m}}\text{Sn}$ source embedded in a CaSnO_3 matrix. The velocity scale was calibrated with the magnetic sextet of a high-purity iron foil as the

reference absorber and ^{57}Co (Rh) as the source. The spectra were fitted with Lorentzian profiles using the least-squares method and the errors regarding the hyperfine parameters were found to be smaller than 0.01 mms^{-1} for the different $\text{Co}_3\text{Sn}_{2-x}\text{In}_x\text{S}_2$ compounds. The total error is estimated to be about 0.03 mm s^{-1} . The isomer shift values are given relative to the δ value of a BaSnO_3 spectrum recorded at room temperature. The absorbers containing 1–2 mg cm^{-2} of ^{119}Sn were prepared inside a glove box under an argon atmosphere. Powder samples were mixed with Apiezon vacuum grease and placed between two Kapton films. The sample holder was then sealed to prevent air contact.

Density functional theory (DFT) calculations were performed using the Vienna Ab-initio Simulation Package (VASP)^{12, 13}, employing the generalized gradient approximation (GGA) with the Perdew-Burke-Ernzerhof (PBE) exchange-correlation functional.¹⁴ A high kinetic energy cut-off of 350 eV (30% above the highest of the standard values for the given set of elements) was used for the planewave expansion of the wavefunctions in order to minimize Pulay stress errors. All calculations were performed on the 21-atom unit cell, and a Gamma-centered grid of $5 \times 5 \times 2$ k-points was employed for Brillouin-zone integrations (test calculations showed that doubling the number of k-points in each direction led to total energy changes of less than 1 meV per formula unit). The ionic positions were relaxed until the forces were negligible (less than 0.01 eV/\AA on each atom). The disordered $\text{Co}_3\text{Sn}_{2-x}\text{In}_x\text{S}_2$ ($0 \leq x \leq 2$) phases were represented by a symmetry-adapted ensemble of configurations, using the methodology implemented in the SOD (Site Occupancy Disorder) program.¹⁵ Fractional site occupancies were then calculated as average values over the ensemble. Full details of the calculations are provided as Supporting Information.

RESULTS AND DISCUSSION

Powder neutron diffraction data from the $2\theta = 156^\circ$, 90° , 63° and 35° banks of the GEM diffractometer were used in a multibank Rietveld refinement performed using the GSAS¹⁶ software package. Refined lattice parameters obtained from powder X-ray diffraction⁷ and the atomic coordinates of $\text{Co}_3\text{Sn}_2\text{S}_2$ reported previously² were used for the initial structural model for Rietveld refinements. Refinements (Figure 2) in the space group $R\bar{3}m$, including lattice parameters, atomic coordinates, thermal parameters and fractional occupancies of the main-group metal site proceeded smoothly, ($R_{\text{wp}} < 3.2\%$, $1.5 \leq \chi^2 \leq 4.2$). Site occupancy factors of the main group atoms were constrained to maintain the overall stoichiometry. Refined parameters are presented in Table 1, whilst selected inter-atomic distances and bond angles are provided as Supporting Information (Table S2).

The c lattice parameter, increases smoothly with increasing indium content (Figure 3), whilst the a lattice parameter initially decreases with increasing levels of indium substitution, until the stoichiometric phase $\text{Co}_3\text{SnInS}_2$ ($x = 1$) is reached. Above this level of substitution, the a lattice parameter is effectively invariant with composition. Lattice parameters for $\text{Co}_3\text{Sn}_2\text{S}_2$, calculated using the PBE correlation function ($a = 5.381 \text{ \AA}$ and $c = 13.166 \text{ \AA}$) are in good agreement with experimentally determined values. Moreover, the compositional dependence of the lattice parameters, calculated using the DFT/SOD approach shows a remarkable level of agreement with experiment, including the discontinuity in gradient of $a(x)$ at $x = 1$ (Figure 3). Whilst the increase of $ca.$ 1.6% in unit

cell volume for complete substitution of tin by indium (Table 1) is consistent with the larger radius of the latter, the compositional dependence of the lattice parameters suggests additional factors may play a role. The principal electronic change across the compositional range is a reduction of two in the valence electron count. Examination of the calculated DOS (Figure 4) indicates that the major contributors to states just below E_F are the $\text{Co-}d_{xy}$ and $\text{Co-}d_{x^2-y^2}$ orbitals, which contribute to the in-plane bonding within the kagome layer. These levels are partially occupied at $x = 0$ and are further depopulated by indium substitution. That this results in a contraction in the a lattice parameter, suggests states in the vicinity of E_F are of anti-bonding character, which is consistent with the partial DOS of Figure 4. At $x = 1$, these states are completely depopulated. Further substitution by indium drives E_F into lower-lying states below the band gap, which are necessarily less anti-bonding in character, whilst leading to occupancy of an increasing fraction of the intra-layer sites by the larger atom. These competing factors may lie behind the effectively constant a lattice parameter at levels of substitution beyond $x = 1$.

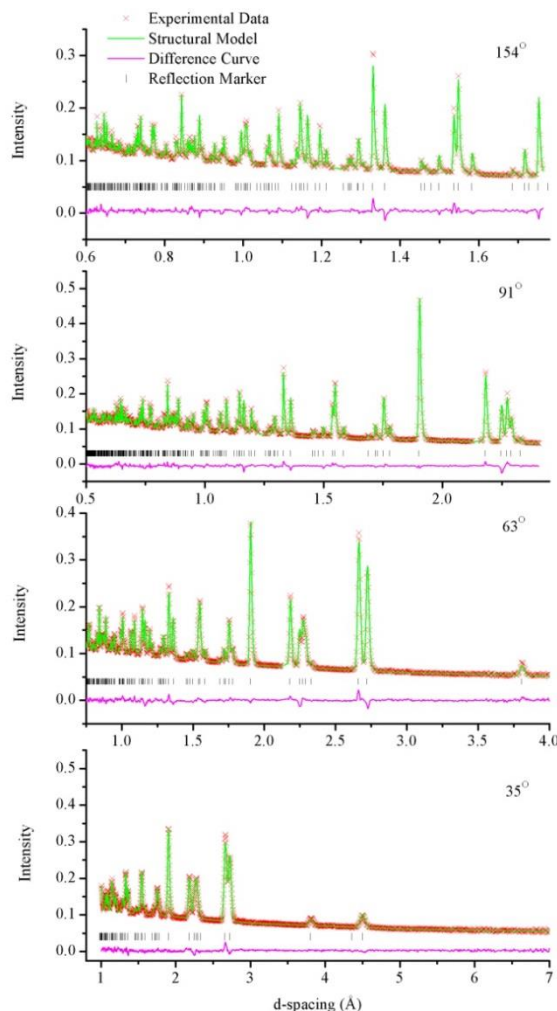


Figure 2. Observed (crosses), calculated (upper full line) and difference (lower full line) neutron diffraction profiles of $\text{Co}_3\text{SnInS}_2$ from each of the four GEM detector banks for refinements carried out for space group $R\bar{3}m$ using data collected at 298 K. Reflection positions are marked and regions where scattering from the vanadium sample can occur are excluded. Profiles for the remaining compositions are provided as Supporting Information.

Table 1. Refined Structural Parameters for $\text{Co}_3\text{Sn}_{2-x}\text{In}_x\text{S}_2$ ($0 \leq x \leq 2$); Space Group $R\bar{3}m$ ^a

x	$a/\text{\AA}$	$c/\text{\AA}$	$\text{Vol}/\text{\AA}^3$	$S(z)$	Co ($U_{\text{iso}}/\text{\AA}^3$)	S ($U_{\text{iso}}/\text{\AA}^3$)	$M(U_{\text{iso}}/\text{\AA}^3)$	SOF In(1) ^b	SOF In(2) ^c
0.0	5.36994(5)	13.1934(3)	329.479(4)	0.28317(7)	0.55(2)	0.64(1)	0.45(2)	0.0(-)	0.0(-)
0.2	5.36088(3)	13.2276(2)	329.217(4)	0.28323(5)	0.62(1)	0.56(1)	0.50(2)	0.087(8)	0.113(8)
0.4	5.34994(3)	13.2925(2)	329.486(4)	0.28205(5)	0.68(2)	0.62(1)	0.58(2)	0.260(6)	0.14(6)
0.6	5.33866(4)	13.3540(2)	329.615(4)	0.28174(6)	0.67(2)	0.63(2)	0.61(2)	0.428(5)	0.172(5)
0.8	5.32480(4)	13.4167(2)	329.444(4)	0.28139(6)	0.61(2)	0.64(2)	0.60(2)	0.604(4)	0.196(4)
1.0	5.31922(4)	13.4799(2)	330.303(5)	0.28108(7)	0.59(2)	0.62(2)	0.54(3)	0.719(4)	0.281(4)
1.2	5.31173(5)	13.5261(2)	330.504(5)	0.28067(7)	0.55(2)	0.62(2)	0.50(3)	0.825(4)	0.375(4)
1.4	5.31489(4)	13.5584(2)	331.686(5)	0.28037(6)	0.50(2)	0.69(2)	0.48(2)	0.869(4)	0.531(4)
1.6	5.31495(4)	13.5909(2)	332.489(5)	0.28027(6)	0.68(7)	0.892(3)	0.63(3)	0.902(4)	0.698(4)
1.8	5.31797(5)	13.6296(2)	333.702(7)	0.27969(8)	0.65(2)	1.06(3)	0.61(3)	0.949(4)	0.851(4)
2.0	5.31811(6)	13.6646(3)	334.689(7)	0.27914(9)	0.74(4)	1.24(4)	0.67(4)	1.0(-)	1.0(-)

^aCo on 9(d), ($\frac{1}{2}$, 0, $\frac{1}{2}$); $M(1)$ on 3(a), (0, 0, 0); $M(2)$ on 3(b) (0, 0, $\frac{1}{2}$); S on 6(c), (0, 0, z);

^bSOF In(1) + SOF Sn(1) = 1.0; ^c SOF In(2) + SOF Sn(2) = 1.0

The behavior of the lattice parameters is reflected in the derived atom-atom distances and angles. In particular, the angle Co- $M(1)$ -Co involving Co in adjacent layers increases with increasing indium content, whilst the Co- $M(1)$ -Co angle involving Co in the same layer decreases. This leads to a narrowing and elongation of the trigonal antiprismatic ($M(1)$) site as indium is introduced. Intralayer Co-Co distances, which are comparable with those observed in the kagome-like network in CoSn (2.639 Å),¹⁷ show a compositional dependence that mirrors that of the a lattice parameter.

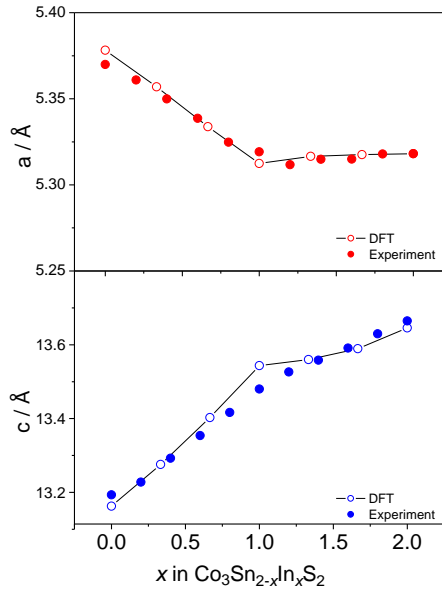


Figure 3. Compositional dependence of lattice parameters of $\text{Co}_3\text{Sn}_{2-x}\text{In}_x\text{S}_2$ determined by powder neutron diffraction compared with the results of DFT calculations. Solid points denote experimental data, open points, the results of calculation. The solid line is intended as a guide to the eye.

Main-group atoms may reside in one of two crystallographically distinct sites in the shandite structure: the inter-layer trigonal antiprismatic sites, $M(1)$, and the $M(2)$ sites located within the kagome layer. Refinement of site occupancy factors using powder neutron diffraction data reveals significant deviations from a statistical distribution of tin and indium atoms over these two sites in the substituted phases (Figure 5). In particular, indium exhibits a marked preference for $M(1)$ sites, the degree of atom partitioning reaching a maximum at $x = 0.8$, where ca. 75% of the available indium atoms reside on $M(1)$ sites. DFT calculations using the SOD treatment lead to excellent agreement of the calculated compositional dependence of the atom distribution with that determined from neutron diffraction (Figure 5).

The origin of the observed site preference may lie in the differing bonding requirements at the two sites. The partial DOS (Figure 4) for the end-member phases indicate the three-fold degeneracy of the p-orbitals associated with the main-group element is removed at both sites. At the inter-layer $M(1)$ site, the p_z orbital lies at a lower energy than the degenerate p_x/p_y pair whilst at the intra-layer $M(2)$ site, this splitting pattern is reversed. At the $M(1)$ site, the p_z orbital participates in two 4-centre bonds with the Co_3 triangles in the two adjacent kagome-like layers, whereas at the $M(2)$ site, intra-layer bonding within the kagome layer, is through six 3-centre M -Co bonds involving the p_x and p_y orbitals of the main-group element. Both indium (three valence electrons) and tin (four valence electrons) are able to satisfy these bonding requirements, even when allowance is made for the charge transfer indicated by the Bader analysis. However, the larger number of bonding interactions associated with the $M(2)$ site in the kagome layer suggests that occupancy by the more electron-rich species (Sn), that is better able to satisfy the bonding through p_x and p_y , is favored. This would account for the observed preferential occupancy of the inter-layer $M(1)$ site by the three-electron species In, which is able to satisfy the bonding requirements at this site through occupation

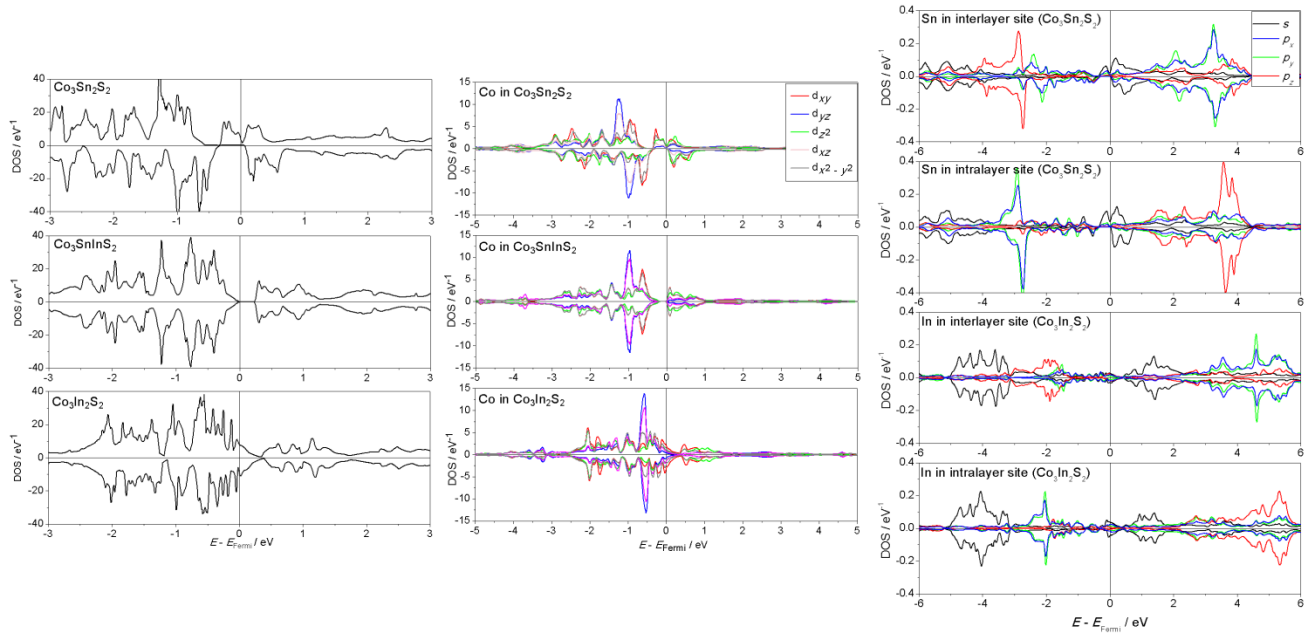


Figure 4: The total (left) and partial (projected on the Co $3d$ orbitals, middle) electronic Density of States (DOS) determined from DFT calculations for $\text{Co}_3\text{Sn}_{2-x}\text{In}_x\text{S}_2$ ($x = 0, 1, 2$). Calculations for $\text{Co}_3\text{SnInS}_2$ were performed for the most energetically favorable configuration. On the right are the partial calculated DOS of the end member ($x = 0, 2$) phases projected on the $5p$ orbitals of the main group element at the interlayer ($M(1)$) and intralayer ($M(2)$) sites

Table 2: Derived magnetic parameters for $\text{Co}_3\text{Sn}_{2-x}\text{In}_x\text{S}_2$ ($0 \leq x \leq 0.4$).

x	$\text{C}/\text{cm}^3 \text{ K mol}^{-1}$	θ/K	$\mu_{\text{eff}}/\mu_{\text{B}}$	T_{C}/K	Range of Fit/K	$M_{\text{sat}}/\mu_{\text{B}}$
0.0	0.47(1)	175(5)	1.12(1)	175(5)	180 - 300	0.632(1)
0.2	0.34(2)	170(2)	0.95(2)	170(1)	220 - 300	0.672(1)
0.4	0.29(1)	135(3)	0.88(1)	135(4)	240 - 300	0.609(2)

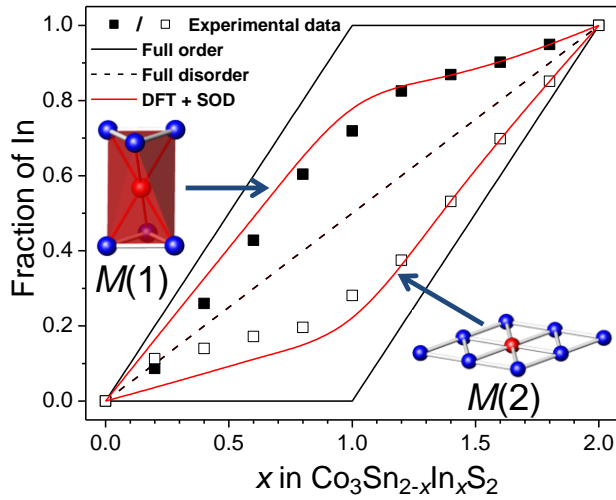


Figure 5. The compositional dependence of indium site occupancy factors associated with the $M(1)$ and $M(2)$ sites in $\text{Co}_3\text{Sn}_{2-x}\text{In}_x\text{S}_2$ ($0 \leq x \leq 2$). Solid and open points denote experimental values for $M(1)$ and $M(2)$ respectively determined from Rietveld refinement and the solid red line, the results from DFT calculations. The variation of site occupancy factors corresponding to full ordering into the $M(1)$ site and to a completely disordered structure are indicated by solid and dashed black lines respectively.

of the p_z orbital but is less effective at the $M(2)$ site. A similar conclusion was recently reached by Rothbaler *et al.*¹⁸ in their

analysis of $\text{Co}_3\text{SnInS}_2$, using a superstructure approach to electronic structure calculation. The incomplete nature of the ordering suggests that the energy differences are small and the observed distribution is the result of incomplete equilibration on cooling from the synthesis temperature.

Zfc and fc magnetic susceptibility data for $\text{Co}_3\text{Sn}_2\text{S}_2$ (Figure 6) overlap each other at higher temperatures, where Curie-Weiss behavior is exhibited. Derived magnetic parameters are presented in Table 2. The positive Weiss constant indicates the dominant exchange interactions are ferromagnetic in origin. The effective magnetic moment is somewhat reduced from the value for the single unpaired electron suggested by band structure calculations. The marked increase observed in zfc and fc data on cooling indicates ferromagnetic order below $T_{\text{C}} = 175$ K, which is also evidenced by the field dependence of the magnetization at 5 K (Figure 7). The saturation magnetization of *ca.* $0.6 \mu_{\text{B}}$, determined by extrapolation to infinite field of the plot of magnetization vs. $1/H$, is lower than the spin-only value for one unpaired electron. This suggests a degree of electron delocalization, consistent with electrical transport properties and the description of this phase as a half-metallic ferromagnet.³ Similar behavior is observed for samples to $x \leq 0.4$ (Figure 6), indicating that half-metallic ferromagnetic behavior persists to this composition. However, with increasing indium content, T_{C} falls until long-range magnetic order is completely suppressed at compositions with $x \geq 0.6$. This behavior may be related to the increasing ($4.682(1)$ Å at $x = 0.4$ to $4.711(1)$ at $x = 0.6$) separation between the kagome-like

Table 3: Binding Energies Determined from X-ray Photoelectron Spectroscopy of $\text{Co}_3\text{Sn}_{2-x}\text{In}_x\text{S}_2$ ($0 \leq x \leq 2$)^a

x	Peak Position/eV		Peak Position/eV		Peak Position/eV		Peak Position/eV
	Co($2p_{3/2}$)	Co($2p_{1/2}$)	Sn($3d_{5/2}$)	Sn($3d_{3/2}$)	In($3d_{5/2}$)	In($3d_{3/2}$)	S($2p$)
0.0	778.5	793.5	486.2	493.7	---	---	163.0
0.4	778.8	793.7	485.5	494.0	444.4	451.9	163.2
1.0	778.7	793.7	485.5	493.9	444.3	451.9	163.1
1.6	778.5	793.4	485.3	493.7	444.1	451.6	162.8
2.0	778.3	793.2	---	---	443.8	451.3	162.5

^a The estimated uncertainty in peak position is ≤ 0.1 eV.

layers as indium is introduced, thereby weakening the interaction between cobalt atoms in adjacent layers. This weakening of inter-layer interactions appears to be sufficient to suppress long-range magnetic order, as evidenced by the almost linear field dependence of the low-temperature magnetization at compositions with $x \geq 0.6$, resulting in magnetic interactions being confined to the two-dimensional kagome-like sheet. As materials become increasingly indium-rich ($x \geq 1.0$), the magnetic susceptibility falls to very low values ($10^{-5} - 10^{-7}$ emu) and becomes effectively independent of temperature (Figure S4). This suggests an increasing degree of electron delocalization, consistent with the electrical transport property data (*vide infra*) leading to Pauli paramagnetism in indium rich phases. The magnetic susceptibility of the end-member phase $\text{Co}_3\text{In}_2\text{S}_2$ is markedly higher (Figure S4), suggesting an increased electron localization, although it remains weakly temperature dependent.

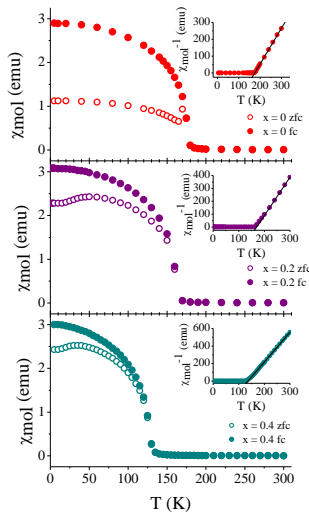


Figure 6. Zero-field-cooled (zfc) and field-cooled (fc) molar magnetic susceptibilities of $\text{Co}_3\text{Sn}_2\text{S}_2$ (top), $\text{Co}_3\text{Sn}_{1.8}\text{In}_{0.2}\text{S}_2$ (middle) and $\text{Co}_3\text{Sn}_{1.6}\text{In}_{0.4}\text{S}_2$ (bottom). Insets show reciprocal susceptibility (fc) data, with the solid line representing the fit to a Curie-Weiss expression.

As indicated above, the formal oxidation state of the elements in such metal-rich phases as the shandites is a matter of some debate. We sought to exploit XPS in an effort to determine the formal oxidation states in the $\text{Co}_3\text{Sn}_{2-x}\text{In}_x\text{S}_2$ series (Figure 8). The binding energies of the Co $2p_{3/2}$ emissions of

$\text{Co}_3\text{Sn}_{2-x}\text{In}_x\text{S}_2$ ($0 \leq x \leq 2$) lie between 778.3 eV and 778.8 eV, whilst those of the Co $2p_{1/2}$ lines are in the range 793.2 eV to 793.7 (Table 3). These values are in good agreement with those of elemental Co ($2p_{3/2} = 778.2$ eV, $2p_{1/2} = 793.3$ eV) and the intermetallic CoNi ($2p_{3/2} = 778.4$ eV, $2p_{1/2} = 793.4$ eV).¹⁹ This suggests that cobalt is in the zero oxidation state throughout the $\text{Co}_3\text{Sn}_{2-x}\text{In}_x\text{S}_2$ ($0 \leq x \leq 2$) series. This is in agreement with conclusions on the oxidation state of nickel in the shandites $\text{Ni}_3\text{M}_2\text{S}_2$ ($M = \text{Sn}, 8 \text{ Pb}^{11}$). A Bader population analysis²⁰ of the electron density obtained from our DFT calculations leads to very small net charges on Co (between 0.03-0.06 depending on composition), supporting the assignment of a formal oxidation state of zero for cobalt.

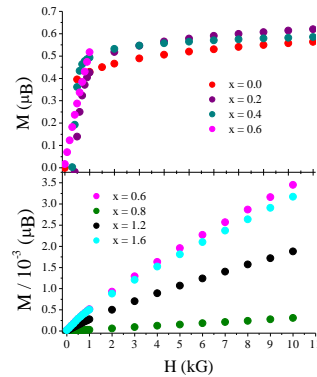


Figure 7. The field dependence of the magnetization of $\text{Co}_3\text{Sn}_{2-x}\text{In}_x\text{S}_2$ at 5 K. Magnetization data for magnetically ordered (upper) and paramagnetic compositions (lower) are presented.

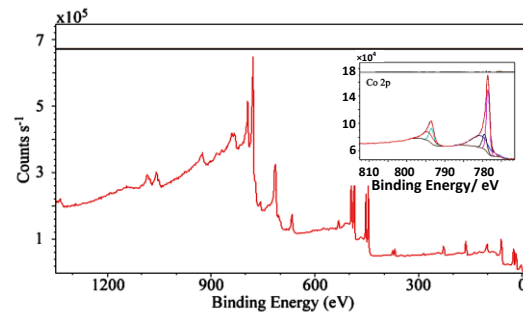


Figure 8. X-ray photoelectron spectroscopy data for $\text{Co}_3\text{Sn}_2\text{S}_2$. The inset shows the fit to the Co($2p$) region of the spectrum.

For the more electronegative element, sulphur, the measured binding energies of the S($2p$) transition lie in the range 162.5 \leq

E_B /eV \leq 163.2 (Table 3). These values are comparable with the majority of reports of the $S(2p)$ binding energy in ternary shandite phases. As has been pointed out by Skinner et al.,¹¹ values in excess of 162 eV are more consistent with metal-rich binary sulphides (pentlandite: 162.2 eV^{21, 22} Ni_3S_2 : 162.2-162.4 eV²³) and even elemental sulphur (163.6 eV²⁴), than those containing the sulphide dianion (SnS: 161.3 eV;²⁵ In_2S_3 : 161.8 eV,²⁶ NiS: 161.7 eV²⁷; CoS: 161.9 eV²⁸), suggesting a low formal oxidation state. Skinner and co-workers have not observed these higher $S(2p)$ binding energies for a $Ni_3Pb_2S_2$ surface prepared by fracturing the sample under UHV and determined a value of 161.5 eV for a $Ni_3Pb_2S_2$, which appears to support a formal valence state of -2. However, they also demonstrated that any increase in the $S(2p)$ binding energy cannot be attributed to aerial oxidation. For the samples investigated here, the XPS data appear to be consistent with a formal oxidation state that approaches zero. Further support for this view is provided by the Bader charge analysis of the DFT calculation, which associates with sulphur a net negative charge of *ca.* 0.7: significantly below 2 and also below the value of *ca.* 1.0 obtained for sulphur in a Bader analysis of solid SnS.

The binding energies measured for the In $3d_{5/2}$ and $3d_{3/2}$ photoemission peaks (Table 3) are in the range $443.8 \leq E_B$ /eV \leq 444.4 and $451.3 \leq E_B$ /eV \leq 451.9 respectively. These compare favorably to those of elemental indium ($3d_{5/2} = 444.0$ eV, $3d_{3/2} = 451.4$ eV) and InSb ($3d_{5/2} = 444.4$ eV).¹⁹ Binding energies for In(III) in In_2S_3 , 444.9 eV (In $3d_{5/2}$) and 452.9 eV (In $3d_{3/2}$),²⁶ are outside the range of values measured here. Therefore comparison with the literature suggests that the formal oxidation state of indium in the substituted shandites approaches zero. The valence state of tin could not be determined from the XPS data as the variation in Sn($3d$) binding energy of Sn(0), Sn(II) and Sn(IV) is small (α -Sn: $3d_{5/2} = 484.9$ eV;¹⁹ $Sn^{II}S$: $3d_{5/2} = 485.9$ eV, $3d_{3/2} = 494.4$ eV)²⁵ and all values are comparable with those measured here for $Co_3Sn_{2-x}In_xS_2$ ($0 \leq x \leq 2$). In order to resolve this ambiguity ^{119}Sn Mössbauer spectroscopy was utilized.

^{119}Sn Mössbauer spectroscopy measurements for $Co_3Sn_2S_2$ (Figure 9) exhibit peaks, with isomer shifts, $\delta = 2.14(1)$, $2.18(1)$ mm s⁻¹, associated with each of two crystallographic sites occupied by tin, with a third much weaker feature ($\delta = -0.19(8)$ mm s⁻¹) corresponding to an oxide impurity (Table 4), not detected by neutron diffraction.

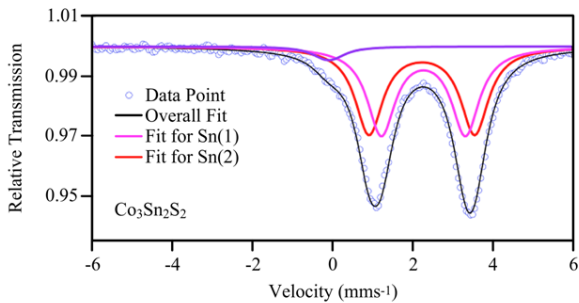


Figure 9. ^{119}Sn Mössbauer spectroscopy data for $Co_3Sn_2S_2$. Points denote experimental data and the full lines signify the fit to the two overlapping doublets and the overall fit. The upper solid line shows the fit to the oxide impurity phase.

The isomer shifts determined here are in good agreement

with those reported by Rothballer et al.⁹ for $Co_3Sn_2S_2$. The peak with the larger quadrupole splitting (Δ) may be assigned to the more distorted crystallographic site, Sn(2), within the kagome-like layer, while the less distorted trigonal antiprismatic Sn(1) site is associated with the peak with the lower Δ . The relative contribution from tin at each of the two crystallographic sites is in good agreement with that expected on the basis of the refined site occupancy factors obtained from powder neutron diffraction data.

Table 4: Isomer shifts (δ), quadrupole splitting (Δ), line width (Γ), the contribution of each line to the spectra and the assignment of the signal to the crystallographic site for ^{119}Sn Mössbauer spectroscopy of $Co_3Sn_{2-x}In_xS_2$ ($0 \leq x \leq 2$).

x	δ (mm/s)	Δ (mm/s)	Γ (mm/s)	Contribution (%)	Assignment
0	-	0.2(1)	0.84(5)	4	oxide
	0.19(8)				
	2.14(1)	2.64(2)	0.84(5)	48	Sn(2)
0.2	2.18(1)	2.10(2)	0.84(5)	48	Sn(1)
	2.14(3)	2.68(7)	0.78(8)	47	Sn(2)
	2.16(3)	2.10(6)	0.78(8)	53	Sn(1)
0.4	2.13(2)	2.62(4)	0.83(8)	67	Sn(2)
	2.16(3)	2.01(6)	0.83(8)	33	Sn(1)
0.6	2.14(2)	2.81(7)	0.82(7)	40	Sn(2)
	2.15(3)	2.27(6)	0.82(7)	60	Sn(1)
0.8	2.14(2)	2.83(3)	0.80(6)	66	Sn(2)
	2.15(2)	2.32(3)	0.80(6)	34	Sn(1)
1	2.11(4)	2.92(8)	0.78(8)	41	Sn(2)
	2.16(3)	2.38(6)	0.78(8)	59	Sn(1)
1.2	2.14(3)	2.76(5)	0.8(1)	77	Sn(2)
	2.15(6)	2.31(9)	0.8(1)	23	Sn(1)
1.6	2.13(3)	2.79(6)	0.8(1)	77	Sn(2)
	2.20(9)	2.1(2)	0.8(1)	23	Sn(1)

The isomer shifts of the two tin resonances differ markedly from the values of 3.40(3) and 1.46 mm s⁻¹ assigned respectively to Sn(II) and Sn(IV) in the mixed-valent $Cr_3Sn_3Se_7$.²⁹ However, the measured values compare favorably with those for tin alloys and intermetallics: Sn^0Mg_2 ($\delta = 1.8$ mm s⁻¹), αSn^0 (2.1 mm s⁻¹), βSn^0 (2.6 mm s⁻¹) and Sn^0Sb (2.8 mm s⁻¹).³⁰ This suggests that the tin atoms in $Co_3Sn_2S_2$ are present in an oxidation state that tends towards zero. The isomer shift of the indium substituted phases (Table 4) lies in a relatively narrow range ($2.15 \leq \delta$ /mm s⁻¹ \leq 2.20 for Sn(1)) and $2.11 \leq \delta$ /mm s⁻¹ \leq 2.14 for Sn(2)). These values are intermediate between those for Sn(II) and Sn(IV), suggesting that the low oxidation state of tin persists throughout the composition range $0 \leq x \leq 2$ of $Co_3Sn_{2-x}In_xS_2$.

Using information from XPS, ^{119}Sn Mössbauer spectroscopy and DFT, we conclude that the oxidation states of the constituent elements in $Co_3Sn_{2-x}In_xS_2$ ($0 \leq x \leq 2$) are substantially reduced from their conventional formal valence state values. That of cobalt appears to be zero, whilst for the other elements present, spectroscopic data indicate oxidation states that ap-

proach zero, although the Bader charge analysis suggests a small degree of charge transfer between the main-group element and sulphur; the maximum extent of which is estimated at $0.7 e^-$, well below that expected for divalent main-group metals and sulphur.

The electrical resistivity of the end-member phase $\text{Co}_3\text{Sn}_2\text{S}_2$ (Figure 10) decreases with decreasing temperature, indicating metallic behavior. Initially, substitution of tin by indium increases the absolute value of the resistivity, whilst retaining the metal-like $\rho(T)$ dependence to compositions, $x = 0.6$. On increasing the indium content towards the semiconducting region ($1 \leq x \leq 1.05$), as defined by previously-reported low temperature measurements,⁷ a change in $\rho(T)$ is observed. In particular, for samples in the compositional regions $0.7 \leq x \leq 0.95$ and $1.1 \leq x \leq 1.2$, the initially positive $d\rho/dT$ changes sign at higher temperatures, indicative of intrinsic semiconducting behavior. The temperature at which the onset of this intrinsic semiconducting behavior is observed, increases with increasing indium content. Materials with compositions corresponding to $x \geq 1.4$ exhibit metallic behavior across the whole measured temperature range. Intriguingly from a thermoelectric perspective, the values of the electrical resistivity of materials in the series are comparable with or lower than those of the candidate thermoelectric materials $\beta\text{-Zn}_3\text{Sb}_4$ ³¹ (2 m Ω cm to 3.5 m Ω cm) and $\text{Yb}_{14}\text{MnSb}_{11}$ ³² (2 m Ω cm to 5.5 m Ω cm).

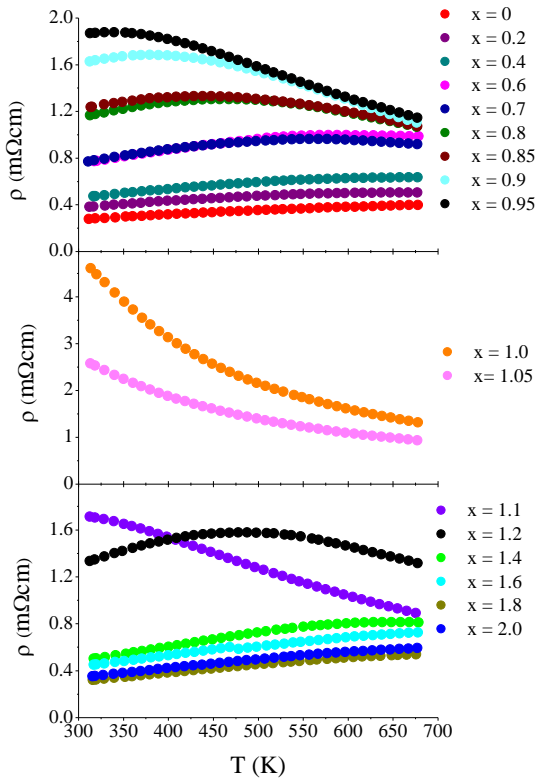


Figure 10. The temperature dependence of the electrical resistivity of phases in the $\text{Co}_3\text{Sn}_{2-x}\text{In}_x\text{S}_2$ ($0 \leq x \leq 2$) series.

Measurements of the Seebeck coefficient at temperatures above ambient (Figure 11) reveal that for compositions corresponding to $x \leq 0.4$, the almost linear $S(T)$ dependence observed at sub-ambient temperatures⁷ persists at higher temper-

atures. However, as the level of indium substitution increases, more complex behavior is observed. In the range $0.7 \leq x \leq 0.95$, the temperature dependence changes so that the absolute value of S decreases with increasing temperature. This is consistent with the change to semiconducting behavior inferred from the $\rho(T)$ dependence of the resistivity data collected at high temperatures. Materials in the region of the stoichiometric composition ($x = 1$), for which resistivity data clearly indicate semiconducting behavior, remain n-type, albeit with an $S(T)$ dependence which is almost invariant with temperature over all or part of the range (Figure 11). The relatively low absolute values of the Seebeck coefficient for the phase with $x = 1.05$ suggests a mixed conduction mechanism of electrons and holes may be operative. This evolution from predominantly n-type behavior continues into $\text{Co}_3\text{Sn}_{0.9}\text{In}_{1.1}\text{S}_2$, which exhibits a change from n- to p-type behavior at 550 K: the strong $S(T)$ dependence suggesting that semiconducting behavior persists to this composition. At higher indium contents, $x > 1.2$, the magnitude of the Seebeck coefficient decreases with indium substitution and the temperature dependence of $S(T)$ weakens markedly, consistent with the metallic $\rho(T)$ dependence.

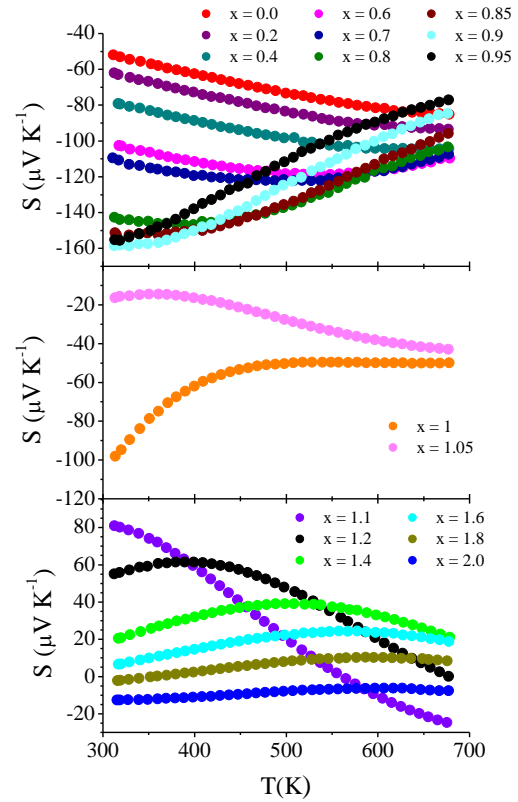


Figure 11. Seebeck coefficient data as a function of temperature for compositions in the $\text{Co}_3\text{Sn}_{2-x}\text{In}_x\text{S}_2$ series ($0 \leq x \leq 2$).

The thermal conductivity (κ) of $\text{Co}_3\text{Sn}_2\text{S}_2$ is almost invariant with temperature (Figure S7), falling in the range 4.5 to 4.7 $\text{W m}^{-1} \text{K}^{-1}$. Introduction of indium leads to a reduction in the thermal conductivity by up to 40 % depending on the indium content: the end-member phase $\text{Co}_3\text{In}_2\text{S}_2$ exhibiting a thermal conductivity comparable with that of $\text{Co}_3\text{Sn}_2\text{S}_2$. By application of the Wiedemann-Franz law ($L = 2.44 \times 10^{-8} \text{ W } \Omega \text{ K}^{-2}$), the

electronic contribution (κ_e) was determined and subtracted from the measured values (κ) to yield the lattice contribution (κ_L). In general κ_e increases with temperature, whilst κ_L remains largely temperature invariant. Examination of the compositional dependence of each of these contributions (Figure 12) at a fixed temperature reveals a broad minimum in thermal conductivity centered on the stoichiometric ($x = 1$) composition. The origin of this appears to lie in the compositional variation of κ_e , which shows a corresponding minimum, in contrast with the much weaker dependence of κ_L on indium content. This is consistent with the expectation that little atomic mass fluctuation scattering is introduced by the partial replacement of tin by indium as these elements differ by only one atomic mass unit.

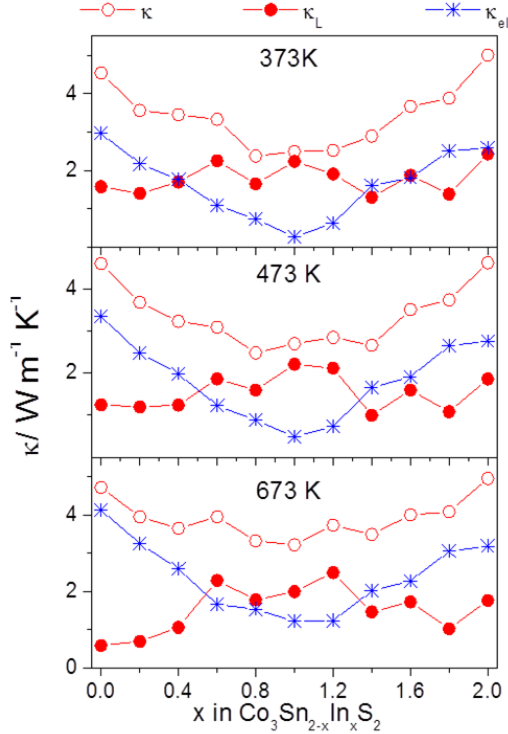


Figure 12. The variation with chemical composition of the overall (κ), electronic (κ_e) and lattice (κ_L) thermal conductivity of $\text{Co}_3\text{Sn}_{2-x}\text{In}_x\text{S}_2$ ($0 \leq x \leq 2$) at 373, 473 and 673 K.

The low values of the thermoelectric figures of merit for indium-rich ($x > 1.0$) members of the $\text{Co}_3\text{Sn}_{2-x}\text{In}_x\text{S}_2$ ($0 \leq x \leq 2$) series (Figure 13) are due principally to the relatively small Seebeck coefficient. However, the tin-rich ($x < 1.0$) members exhibit more promising behavior. The compositional dependence of the maximum ZT and the temperature at which it occurs is presented in Figure 14. The overall highest figure of merit in the series is $ZT = 0.32$ determined for $\text{Co}_3\text{Sn}_{1.6}\text{In}_{0.4}\text{S}_2$ at 673 K.

There have been a number of recent investigations on sulphide thermoelectrics motivated by the search for a tellurium-free replacement for Bi_2Te_3 . Amongst conventional bulk materials, the Chevrel phase $\text{Cu}_4\text{Mo}_6\text{S}_8$,³³ $\text{LaGd}_{1.03}\text{S}_3$ ³⁴ and Cu_yTiS_2 ³⁵ have been reported to exhibit $ZT \geq 0.4$, albeit at temperatures higher than the maximum at which the properties of $\text{Co}_3\text{Sn}_{2-x}\text{In}_x\text{S}_2$ have been investigated here. However, the maximum ZT of 0.32 at 673 K for $\text{Co}_3\text{Sn}_{1.6}\text{In}_{0.4}\text{S}_2$ compares

favorably with that of Cu_yTiS_2 at the same temperature and is slightly higher than that of both $\text{Cu}_4\text{Mo}_6\text{S}_8$ and $\text{LaGd}_{1.03}\text{S}_3$. Moreover, $ZT = 0.28$ for $\text{Co}_3\text{Sn}_{2-x}\text{In}_x\text{S}_2$ ($0.8 \leq x \leq 0.85$) at ca. 425 K is 50% higher than that of Cu_yTiS_2 , double that of $\text{Cu}_4\text{Mo}_6\text{S}_8$ and nearly three times the value reported for $\text{LaGd}_{1.03}\text{S}_3$ at the same temperature.

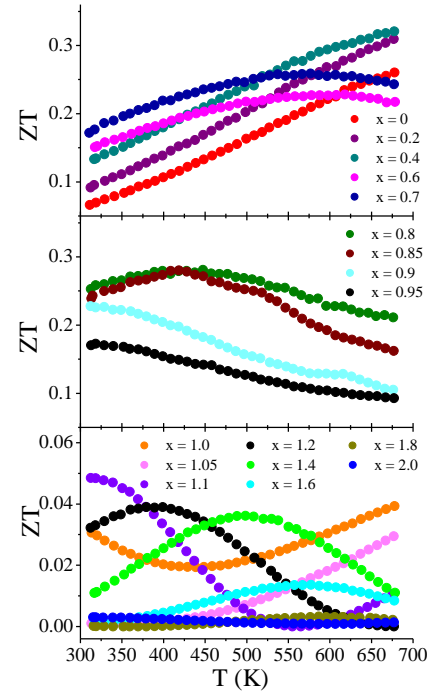


Figure 13. Temperature dependence of the thermoelectric figure of merit, ZT, for $\text{Co}_3\text{Sn}_{2-x}\text{In}_x\text{S}_2$ ($0 \leq x \leq 2$).

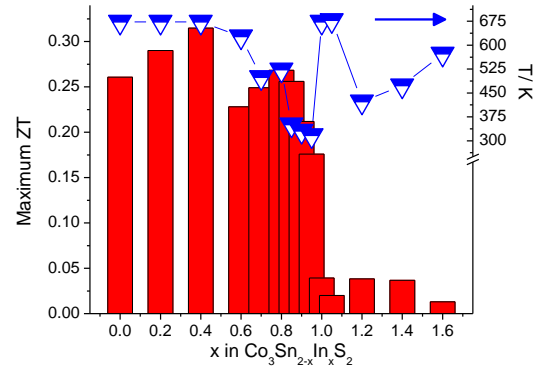


Figure 14. The maximum ZT of $\text{Co}_3\text{Sn}_{2-x}\text{In}_x\text{S}_2$ as a function of composition. The maximum ZT is indicated by the solid bars and the corresponding temperature at which this maximum occurs is denoted by the triangular points.

CONCLUSIONS

The shandite structure is retained at all levels of indium substitution in the series $\text{Co}_3\text{Sn}_{2-x}\text{In}_x\text{S}_2$ ($0 \leq x \leq 2$), with indium preferentially occupying the inter-layer $M(1)$ site over the $M(2)$ kagome layer site. This is supported by DFT calculations which confirm that the partially ordered structures of the quaternary phases, determined by powder neutron diffraction, correspond to the lowest energy arrangements. The half metal-

lic ferromagnetism of the end-member $\text{Co}_3\text{Sn}_2\text{S}_2$ introduces anomalies into $\rho(T)$ and $S(T)$ at the ferromagnetic ordering temperature.² Similar features are present at levels of indium incorporation below $x = 0.4$,⁷ which together with the $\chi(T)$ behavior reported here, suggest that long-range magnetic order persists in this range of composition. The suppression of magnetic order above $x = 0.4$ may be related to the weakening of interlayer exchange interactions due to increasing separation between the kagome layers with increasing indium content.

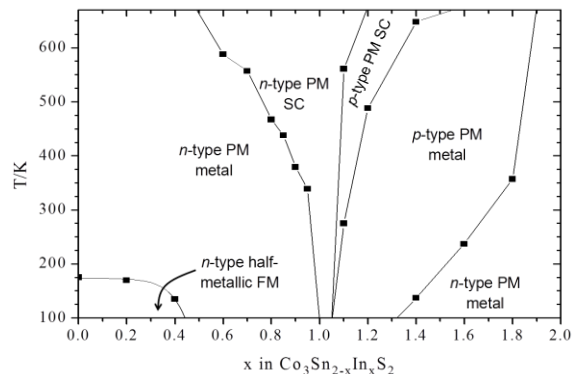


Figure 15: Magnetic and electrical transport properties of $\text{Co}_3\text{Sn}_{2-x}\text{In}_x\text{S}_2$ as a function of composition in the range $0 \leq x \leq 2$ and temperature in the range $100 \leq T/\text{K} \leq 673$, incorporating data from Reference 6 together with those of the present study. (PM, paramagnet; FM, ferromagnet; SC, semiconductor).

Data from a combination of spectroscopic techniques reveal that the oxidation states of the constituent elements are or approach zero; a maximum charge transfer of *ca.* $0.7 e^-$ between the main-group elements and sulphur being indicated by the DFT calculations. This suggests that the members of this series possess characteristics more akin to intermetallic materials than conventional ionic-covalent compounds and the position of the Fermi level (E_F) is best characterized by consideration of the total electron count. E_F has been progressively lowered through the chemical substitution of tin by indium, which removes one electron for each tin atom substituted. This has been used to effect changes to the electron transport properties, leading to an unusual double metal-to-semiconductor-to-metal electronic transition with increasing indium content. Band structure calculations reveal the presence of relatively sharp narrow bands in the vicinity of E_F and the tuning of E_F through such a highly structured region of the DOS leads to a marked increase in the Seebeck coefficient as the stoichiometric phase $\text{Co}_3\text{SnInS}_2$ is approached. The semiconducting properties of this phase may be understood in terms of an overall electron count which leads to a completely filled band. The increase in electrical resistivity at this composition appears to be responsible for the minimum in thermal conductivity, the compositional dependence of which is dominated by the electronic contribution. Materials with compositions either side of $\text{Co}_3\text{SnInS}_2$ that exhibit a metallic $\rho(T)$ dependence at low temperatures display intrinsic semiconductor behavior upon heating. Seebeck coefficient measurements suggest that materials in this region are mixed conductors in which both electrons and holes play a role; the sign of the measured Seebeck coefficient being both composition and temperature dependent. The magnetic, and electrical transport properties of $\text{Co}_3\text{Sn}_{2-x}\text{In}_x\text{S}_2$ may be summarized in the form of an electronic

“phase diagram” (Figure 15). The compositional tuning of electrical transport properties by varying E_F in a region where the electronic density of states is highly structured, produces a 3-fold increase in the figure-of-merit of $\text{Co}_3\text{Sn}_{1.2}\text{In}_{0.8}\text{S}_2$ (at 425 K) over that of the ternary end-member phase, indicating that tuning of E_F to a discontinuity in $N(E)$ is effective in enhancing the thermoelectric response. The maximum $ZT = 0.32$ observed for $\text{Co}_3\text{Sn}_{1.6}\text{In}_{0.4}\text{S}_2$ at high temperatures is competitive with other sulphide materials recently investigated. Moreover, the remarkably high power factors of up to $20 \mu\text{W cm}^{-1} \text{K}^{-2}$ determined for phases with $x < 1$ are of the same order as those of bismuth tellurides, which exhibit power factors of 28, 49 and $56 \mu\text{W cm}^{-1} \text{K}^{-2}$ in bulk nanostructured,³⁶ thin-film³⁷ and single-crystal³⁸ forms respectively. The promising electrical performance of $\text{Co}_3\text{Sn}_{2-x}\text{In}_x\text{S}_2$ suggests that further optimization for applications in low-grade waste-heat recovery may be possible through for example, nanostructuring, to effect reductions in thermal conductivity.

ASSOCIATED CONTENT

Magnetic susceptibility data, neutron profiles, thermal conductivity data, refined bond lengths and angles, X-ray photoelectron and Mössbauer spectroscopic data and details of the DFT/SOD calculation methodologies. This information is available free of charge via the Internet at <http://pubs.acs.org>

AUTHOR INFORMATION

Corresponding Author

* E-mail: a.v.powell@reading.ac.uk

* E-mail: p.vaqueiro@reading.ac.uk

Author Contributions

The manuscript was written through contributions of all authors. All authors have given approval to the final version of the manuscript.

Funding Sources

UK Engineering and Physical Sciences Research Council; UK Science and Technology Facilities Council.

ACKNOWLEDGMENT

X-ray photoelectron spectra were obtained at the National EPSRC XPS Users' Service (NEXUS) at Newcastle University, an EPSRC Mid-Range Facility. The authors wish to thank Dr Anders Barlow for performing these measurements.

REFERENCES

- 1 Range, K.; Rau, F.; Zabel, M.; Paulus, H. Crystal Structure of Nickel Tin Sulfide (3/2/2), $\text{Ni}_3\text{Sn}_2\text{S}_2$. *Z. Kristallogr.* **1997**, *212*, 50-50.
- 2 Vaqueiro, P.; Sobany, G. G. A Powder Neutron Diffraction Study of the Metallic Ferromagnet $\text{Co}_3\text{Sn}_2\text{S}_2$. *Solid State Sci.* **2009**, *11*, 513-518.
- 3 Wehrich, R.; Anusca, I. Half Antiperovskites. III - Crystallographic and Electronic Structure Effects in $\text{Sn}_{2-x}\text{In}_x\text{Co}_3\text{S}_2$. *Z. Anorg. Allg. Chem.* **2006**, *632*, 1531-1537.
- 4 Hicks, L.D.; Dresselhaus, M.S. Effect of Quantum-Well Structures on the Thermoelectric Figure of Merit. *Phys. Rev. B*, **1993**, *47*, 12727-12731.

- 5 Mott, N. F.; Davis, E. A., *Electronic processes in non-crystalline materials*. 2d ed.; Clarendon Press; Oxford University Press: Oxford, New York, 1979;
- 6 Vaqueiro, P.; Powell, A.V. Recent Developments in Nanostructured Materials for High-Performance Thermoelectrics. *J. Mater. Chem.* **2010**, *20*, 9577-9584.
- 7 Corps, J.; Vaqueiro, P.; Powell, A. V. $\text{Co}_3\text{M}_2\text{S}_2$ (M = Sn, In) Shandites as Tellurium-Free Thermoelectrics. *J. Mater. Chem. A* **2013**, *1*, 6553-6557.
- 8 Gutlich, P.; Range, K. J.; Felser, C.; Schultz-Munzenberg, C.; Tremel, W.; Walcher, D.; Waldeck, M. The Valence States of Nickel, Tin, and Sulfur in the Ternary Chalcogenide $\text{Ni}_3\text{Sn}_2\text{S}_2$ - XPS, ^{61}Ni and ^{119}Sn Mössbauer Investigations, and Band Structure Calculations. *Angew. Chem. Int. Ed.* **1999**, *38*, 2381-2384.
- 9 Rothballer, J.; Bachhuber, F.; Pielhofer, F.; Schappacher, F. M.; Pöttgen, R.; Wehrich, R. Effect of In-Sn Ordering on Semiconducting Properties in $\text{InSnCo}_3\text{S}_2$ - X-ray, ^{119}Sn Mössbauer Spectroscopy, and DFT Studies. *Eur. J. Inorg. Chem.* **2013**, 248-255.
- 10 Umetani, A.; Nagoshi, E.; Kubodera, T.; Matoba, M. Electronic and Magnetic Nature of Shandite-Type $\text{A}_2\text{Co}_3\text{S}_2$ (A = Sn, In). *Physica B*, **2008**, *403*, 1356-1358.
- 11 Skinner, W. M.; Qian, G.; Buckley, A. N. Electronic Environments in $\text{Ni}_3\text{Pb}_2\text{S}_2$ (Shandite) and its Initial Oxidation in Air. *J. Solid State Chem.* **2013**, *206*, 32-37.
- 12 Kresse, G.; Furthmüller, J. Efficiency of Ab-Initio Total Energy Calculations for Metals and Semiconductors Using a Plane-Wave Basis Set. *Comput. Mater. Sci.* **1996**, *6*, 15-50.
- 13 Kresse, G.; Furthmüller, J. Efficient Iterative Schemes for Ab Initio Total-Energy Calculations Using a Plane-Wave Basis Set. *Phys. Rev. B* **1996**, *54*, 11169-11186.
- 14 Perdew, J. P.; Burke, K.; Ernzerhof, M. Generalized Gradient Approximation Made Simple. *Phys. Rev. Lett.* **1996**, *77*, 3865-3868.
- 15 Grau-Crespo, R.; Hamad, S.; Catlow, C. R. A.; de Leeuw, N. H. Symmetry-Adapted Configurational Modelling of Fractional Site Occupancy in Solids. *J. Phys.: Condens. Matter* **2007**, *19*, 256201.
- 16 Larson, A. C.; von Dreele, R. B. General Structure Analysis System (GSAS), Los Alamos National Laboratory Report LAUR 86-748, 2004.
- 17 Larsson, A. K.; Haeberlein, M.; Lidin, S.; Schwarz, U. Single Crystal Structure Refinement and High-Pressure Properties of CoSn . *J. Alloy. Compd.* **1996**, *240*, 79-84.
- 18 Rothballer, J.; Bachhuber, F.; Rommel, S.M.; Söhnle, T.; Wehrich, R. Origin and Effect of In-Sn Ordering in $\text{InSnCo}_3\text{S}_2$: A Neutron Diffraction and DFT study. *RSC Adv.* **2014**, *4*, 42183-42189.
- 19 NIST X-ray Photoelectron Spectroscopy Database, Version 4.1 (National Institute of Standards and Technology, Gaithersburg, 2012); <http://srdata.nist.gov/xps/>.
- 20 Bader, R. F. W., *Atoms in Molecules: A Quantum Theory*. Oxford University Press: 1994.
- 21 Buckley, A.N.; Woods, R. Surface-Composition of Pentlandite Under Flotation-Related Conditions. *Surf. Interface Anal.* **1991**, *17*, 675-680.
- 22 Goh, S.W.; Buckley, A.N.; Lamb, R.N.; Fan, L.-J.; Jang, L.-Y.; Yang, Y.-W. Pentlandite Sulfur Core Electron Binding Energies. *Phys. Chem. Miner.* **2006**, *33*, 445-456.
- 23 Buckley, A.N.; Woods, R. Electrochemical and XPS Studies of the Surface Oxidation of Synthetic Heazlewoodite (Ni_3S_2). *J. Appl. Electrochem.* **1991**, *21*, 575-582.
- 24 Peisert, H.; Chassé, T.; Streubel, P.; Meisel, A.; Szargan, R. Relaxation Energies in XPS and XAES of Solid Sulfur-Compounds. *J. Electron Spectrosc.* **1994**, *68*, 321-328.
- 25 Ramakrishna Reddy, K. T.; Purandar Reddy, P.; Miles, R. W.; Datta, P. K. Investigations on SnS Films Deposited by Spray Pyrolysis. *Opt. Mater.* **2001**, *17*, 295-298.
- 26 Kumar, P. M. R.; John, T. T.; Kartha, C. S.; Vijayakumar, K. P.; Abe, T.; Kashiwaba, Y. Effects of Thickness and Post Deposition Annealing on the Properties of Evaporated In_2S_3 Thin Films. *J. Mater. Sci.* **2006**, *41*, 5519-5525.
- 27 Goh, S.W.; Buckley, A.N.; Lamb, R.N.; Skinner, W.M.; Pring, A.; Wang, H.; Fan, L.-J.; Jang, L.-Y.; Lai, L.-J.; Yang, Y.-W. Sulfur Electronic Environments in α -NiS and β -NiS: Examination of the Relationship Between Coordination Number and Core Electron Binding Energies. *Phys Chem Minerals* **2006**, *33*, 98-105.
- 28 Battistoni, C.; Gastaldi, G.; Mattogno, G.; Simeone, M. G.; Viticoli, S. Structural and Magnetic Properties of Layer Compounds - CoGaInS_4 . *Solid State Commun.* **1987**, *61*, 43-46.
- 29 Bodenau, F.; Cajipe, V.; Danot, M.; Ouvrard, G. Spin-Glass-Like Behavior in the Selenide $\text{Cr}_2\text{Sn}_3\text{Se}_7$. *J. Solid State Chem* **1998**, *137*, 249-254.
- 30 Lippens, P. E. Interpretation of the ^{119}Sn Mössbauer Isomer Shifts in Complex Tin Chalcogenides. *Phys. Rev. B* **1999**, *60*, 4576-4586.
- 31 Caillat, T.; Fleurial, J. P.; Borshchevsky, A. Preparation and Thermoelectric Properties of Semiconducting Zn_4Sb_3 . *J. Phys. Chem. Solids* **1997**, *58*, 1119-1125.
- 32 Brown, S.; Kaulzarich, S.; Gascoin, F.; Snyder, G. $\text{Yb}_{14}\text{MnSb}_{11}$: New High Efficiency Thermoelectric Material for Power Generation. *Chem. Mater.* **2006**, *18*, 1873-1877.
- 33 Ohta, M.; Obara, H.; Yamamoto, A. Preparation and Thermoelectric Properties of Chevrel-Phase $\text{Cu}_x\text{Mo}_6\text{S}_8$ ($2.0 \leq x \leq 4.0$). *Mater. Trans.* **2009**, *50*, 2129-2133.
- 34 Ohta, M.; Hirai, S.; Kuzuya, T. Preparation and Thermoelectric Properties of $\text{LaGd}_{1+x}\text{S}_3$ and $\text{SmGd}_{1+x}\text{S}_3$. *J. Electron. Mater.* **2011**, *40*, 537-542.
- 35 Guilmeau, E.; Bréard, Y.; Maignan, A. Transport and Thermoelectric Properties in Copper intercalated TiS_2 Chalcogenide. *Appl. Phys. Lett.* **2011**, *99*, 052107.
- 36 Saleemi, M.; Toprak, M.S.; Li, S.; Johnsson, M.; Muhammed, M. Synthesis, Processing, and Thermoelectric Properties of Bulk Nanostructured Bismuth Telluride (Bi_2Te_3). *J. Mater. Chem.*, **2012**, *22*, 725-730.
- 37 Goncalves, L.M.; Couto, C.; Alpuim, P.; Rolo, A.G.; Völklein, F.; Correia, J.H. Optimization of Thermoelectric Properties on Bi_2Te_3 Thin Films Deposited by Thermal Co-Evaporation. *Thin Solid Films*, **2010**, *518*, 2816-2821.
- 38 Scherrer, H.; Scherrer, S. Thermoelectric Properties of Bismuth Antimony Telluride Solid Solutions. In *CRC Handbook of Thermoelectrics*; Rowe, D.M., Ed.; CRC, Boca Raton, 2006, p. 27-1.

Table of Contents Graphic

